scientific reports

OPEN

Exploiting spinel manganese oxide decorated with silver nanoparticles as electrodes for supercapacitor application

Monika Michalska[1]✉, Martin Sarman[1], Janhavi Sharma[2], Chandini Kumar[2], Kamil Sobczak[3], Pramod Kumar Singh[4] & Amrita Jain[2]✉

This work presents a novel approach to the development of supercapacitor technology through the integration of a gel polymer electrolyte (GPE) and Ag nanoparticle (NP) modified Mn_3O_4 electrodes. To the best of our knowledge, this is the first study to employ a GPE comprising poly(vinylidene fluoride)-co-hexafluoropropylene (PVdF-HFP) as the host polymer, propylene carbonate (PC) as the plasticizer, and magnesium perchlorate ($Mg(ClO_4)_2$) as the salt, in conjunction with Ag NP-modified Mn_3O_4 electrodes. The study also introduces a pioneering low-temperature ultrasonication method for the attachment of Ag NPs to Mn_3O_4, which eliminates the need for a reducing agent. This approach is characterized by its simplicity, cost-effectiveness, and scalability, offering significant advantages over conventional methods. The electrochemical performance of the resulting supercapacitor cells, featuring the modified electrodes and novel GPE, was comprehensively evaluated, yielding a single electrode specific capacitance of 9.38 F g^{-1}, with an energy density of 1.9 Wh kg^{-1}, and a power density of 30.8 W kg^{-1}. The findings demonstrate the potential of this new system to enhance energy storage capabilities, marking a substantial advancement in supercapacitor research, and this study sets the foundation for future investigations into scalable, high-performance energy storage solutions, emphasizing both innovation in material design and process optimization.

Keywords Manganese oxide, Mn_3O_4, Silver nanoparticles, Ag, Gel polymer electrolyte, Supercapacitor

The use of supercapacitors is becoming increasingly prevalent in a variety of applications that require the delivery or storage of energy rapidly and efficiently. These include regenerative braking systems in electric vehicles, backup power systems, and a variety of consumer electronics, where the ability to rapidly charge and discharge is crucial. Furthermore, supercapacitors are being employed in renewable energy systems to mitigate fluctuations in power output[1,2]. Supercapacitors, also called ultracapacitors, are energy storage devices that are capable of storing and delivering energy at a considerably faster rate than conventional batteries[1,2]. They can be classified into two primary categories: electrochemical double-layer capacitors (EDLCs) and pseudocapacitors. EDLCs utilize electrostatic charge separation at the interface between an electrode and an electrolyte to store energy, whereas pseudocapacitors employ faradaic redox reactions involving electron transfer to achieve energy storage[2,3]. The materials most commonly utilized as electrodes in supercapacitors include activated carbon (employed in EDLCs due to their elevated surface area), metal oxides (such as RuO_2 and MnO_2), and conducting polymers (including polyaniline and polypyrrole), which are frequently used in pseudocapacitors due to their ability to undergo reversible redox reactions[2,3].

Transition metal oxides have been the subject of considerable research interest as electrode materials for supercapacitors, due to their high theoretical capacitance, excellent electrochemical stability, and environmentally benign nature[2–6]. Among these, manganese oxides (MnO_2, Mn_3O_4, etc.) are of particular interest due to their low cost, natural abundance, and multiple oxidation states, which facilitate efficient redox reactions and are therefore essential for high energy and power density[7,8].

[1]Department of Chemistry and Physico-Chemical Processes, Faculty of Materials Science and Technology, VSB – Technical University of Ostrava, 17. listopadu 2172/15, Ostrava-Poruba 708 00, Czech Republic. [2]Institute of Fundamental Technological Research, Polish Academy of Sciences, Pawińskiego 5B, Warsaw 02-106, Poland. [3]Faculty of Chemistry, Biological and Chemical Research Centre, University of Warsaw, Żwirki i Wigury 101, Warsaw 02-089, Poland. [4]Center for Solar Cells and Renewable Energy (CSRE), Department of Physics, SSBSR, Sharda University, Greater Noida 201310, India. ✉email: monika.kinga.michalska@gmail.com; ajain@ippt.pan.pl

Manganese oxide in the form of Mn_3O_4, a mixed-valence compound containing Mn^{2+} and Mn^{3+} ions, has been identified as a promising candidate for use in supercapacitor electrodes. Mn_3O_4 exhibits notable electrochemical properties, including a high specific capacitance, which is a consequence of its unique spinel structure (where Mn^{2+} ions occupy the tetrahedral site and Mn^{3+} ions occupy the octahedral site of the crystal structure) that provides abundant active sites for intercalation and deintercalation of ions[7,8]. Various synthesis techniques have been utilized with the objective of optimizing the morphology, surface area, and crystalline structure of Mn_3O_4, each contributing to the electrochemical performance of the material[8–12]. The most prevalent techniques employed for the synthesis of Mn_3O_4 encompass hydrothermal, sol-gel, and co-precipitation methodologies, among others[8–12]. Li et al.[9] designed a straightforward one-step hydrothermal process to facilitate the growth of Mn_3O_4 nanorods on Ni foam. The resulting nanorods, with diameters of approximately 100 nm and lengths between 2 and 3 µm, demonstrated a notable specific capacitance of 263 F g^{-1} at 1 A·g^{-1}[9]. The electrochemical performances were realized in a three-electrode system, with 4 M NaOH liquid electrolyte solution[9]. Raj and co-authors[10] investigated a facile synthesis of Mn_3O_4 nanoparticles at room temperature via a simple chemical precipitation method. The electrochemical performance of Mn_3O_4 nanoparticles yielded a specific capacitance of 322 F g^{-1} at 0.5 mA cm^{-2}, a good rate capability of 223 Fg^{-1} at 15 mA cm^{-2}, as well as a notable cycling life, with capacitance retention at 77% after 1000 cycles[10]. Luo et al.[11] proposed a simple method to fabricate Mn_3O_4 cubes, which, on electrochemical examinations, delivered an excellent specific capacitance of 667 F g^{-1}. at a scan rate of 1 mV s^{-1}, 583 F g^{-1} at a low current density of 1 A g^{-1}, respectively. The EIS tests were performed in a three-electrode system, utilizing a 6 M KOH liquid electrolyte solution[11]. Fang et al.[12] employed a colloidal method to synthesize ultrafine Mn_3O_4 nanowires, resulting in a specific capacitance of 433.1 F g^{-1} at a current density of 0.5 A g^{-1}, with a voltage range from −0.5 to 1.1 V in a 1 M Na_2SO_4 electrolyte, in a three-electrode system cell examination. The material was also tested in two configurations, using a cathode electrode consisting of ultrafine Mn_3O_4 nanowires and an active carbon (AC) anode electrode[12]. The constructed device exhibited a high energy density of 26.7 Wh kg^{-1} at a power density of 442 W kg^{-1}, and revealed excellent cycling stability, retaining 75.8% of its initial capacitance value after 64,000 charge/discharge cycles[12].

However, the intrinsic conductivity of Mn_3O_4 is relatively low, which can limit its overall electrochemical performance[7–12]. In this regard, substantial research has been undertaken into surface modification strategies to address this limitation. These strategies involve the incorporation of conductive additives, the creation of composite structures, or doping with other elements to enhance electrical conductivity and electrochemical activity. The modifications can considerably improve charge transfer kinetics, cycling stability, and specific capacitance. For instance, Cuéllar-Herrera et al.[13] employed milling and ultrasonic processes to fabricate Mn_3O_4/rGO composites. A composition of 70% Mn_3O_4 and 30% rGO exhibited a specific capacitance value of 525 Fg^{-1} at 5 mV s^{-1} in a three-electrode cell[13]. The material was also examined in a symmetrical configuration, demonstrating a stability of 85% after 5000 charge-discharge cycles. The specific energy density was found to be 6.25 Wh kg^{-1} at a power density of 125 Wh kg^{-1} and a current density of 0.5 Ag^{-1}, and 5.36 Wh kg^{-1} at a power density of 500 Wh kg^{-1} and a current density of 2 A g^{-1}[13]. A facile one-step solvothermal process was proposed to obtain a flowerlike Mn_3O_4/rGO compound by Zhang et al.[14]. The electrochemical evaluation was done in a three-electrode system using 2 M KOH liquid electrolyte, in which the Mn_3O_4/rGO electrode displayed a high specific capacity of 118.4 mAh g^{-1} at a current density of 1 A g^{-1}, accompanied by an excellent cycling stability of 88.1% after 4000 cycles at a current density of 10 A g^{-1}[14].

In a recent study, Chinnaiah and colleagues[15] employed a green sol-gel synthesis involving an extract of Withania somnifera to synthesize an Ag/Mn_3O_4 nanocomposite. The achieved Ag/Mn_3O_4 electrode was examined in 1 M KOH liquid electrolyte and revealed a specific capacitance of 338 F g^{-1} at a current density of 1 A g^{-1}, with a cyclic retention of 87.4%[15].

The objective of this study is to examine the influence of modifying the surface of manganese oxide (Mn_3O_4) with a spinel structure through the incorporation of silver nanoparticles (Ag NPs) on its energy storage potential. Building on our prior works, in which we successfully demonstrated the surface modification of activated carbon[16], multiwalled carbon nanotubes[17], and cobalt oxide[5] with Ag NPs for use as electrode materials in symmetric supercapacitor configurations, the current research offers a novel extension of this approach. Our previous studies demonstrated that the integration of Ag NPs significantly enhanced the electrochemical performance of these materials, reinforcing the effectiveness of our methodology.

This study introduces a novel application of a gel polymer electrolyte (GPE) for the evaluation of supercapacitor performance. To the best of our knowledge, this represents the first investigation utilizing a GPE composed of poly(vinylidene fluoride-co-hexafluoropropylene) (PVdF-HFP) as the host polymer, propylene carbonate (PC) as the plasticizer, and magnesium perchlorate ($Mg(ClO_4)_2$) as the conducting salt, in combination with manganese oxide (Mn_3O_4) electrodes modified with silver nanoparticles (Ag NPs). In addition, a new low-temperature ultrasonication technique was developed to modify the surface of Mn_3O_4 with Ag NPs, eliminating the need for chemical reducing agents. This approach is notable for three features: its operational simplicity, direct approach, and cost-effectiveness. Collectively, these characteristics contribute to its potential as a viable pathway for scalable synthesis. The resulting supercapacitor devices, incorporating both the modified electrodes and the novel GPE, were subjected to comprehensive electrochemical characterization, signifying a substantial contribution to the advancement of energy storage technologies.

Experimental details

Materials used

Manganese oxide (Mn_3O_4, 97%), poly(vinylidene fluoride-hexafluoropropylene) (PVDF-HFP, > 99.9%) were purchased from Sigma-Aldrich. Silver nitrate ($AgNO_3$) and ethanol (96%) were procured from Lachema. Activated carbon (Activated charcoal) was purchased from CHEMPUR. All chemicals used were of analytical grade and were used as received.

Preparation of Mn_3O_4@Ag composites

The manganese oxide material was surface modified with 1, 3, and 5 wt% Ag nanoparticles using the procedure described below. Silver nitrate ($AgNO_3$, pure p.a., Lachema) was first dissolved in 50 mL of ethanol (96%, Lachema). Subsequently, manganese oxide (Mn_3O_4, Sigma-Aldrich) was introduced to the nitrate–ethanol solution of Ag that had been prepared previously. The synthesis was conducted in an ultrasonic bath cleaner for 2 h, with 30 min of sonication separated by 30 min intervals. The dark-brown suspension was then air-dried for several hours at temperatures ranging from 60 °C to 150 °C for several hours. In the final stage of the procedure, the manganese oxide materials with 1, 3, and 5 wt% of silver were ground in an agate mortar to achieve a fine powder. Figure 1 presents the synthesis procedure of Mn_3O_4@Ag composites, along with the proposed mechanism for the reduction of $AgNO_3$ without the need for a reducing agent. The precise pathway governing the nucleation and growth of silver nanoparticles under these conditions remains to be fully elucidated. Given that no chemical reducing agents were employed and that the materials were not exposed to the elevated temperatures typically required for the complete thermal decomposition of silver nitrate, it is hypothesized that the Mn_3O_4@Ag composite itself may have played a direct role in facilitating the reduction of Ag^+ ions. Furthermore, it is proposed that this reduction process occurred in parallel with the photolysis and/or partial thermal decomposition of $AgNO_3$, potentially enhanced by the ultrasonication treatment applied during synthesis. The resulting samples were labelled M1, M3, and M5, and a control sample without Ag nanoparticles was labelled M0 (Mn_3O_4).

Characterization

The X-ray diffractometry (XRD) was performed on a Panalytical X'Pert Pro MPD (Multipurpose Diffractometer). Data collection was performed over a range from 10 to 90° with a scanning rate of 1.5° (2θ)/min with CuKα radiation (45 kV, 40 mA, $\lambda = 1.5406$ nm). The crystal phases were identified by referencing diffraction patterns in a licensed library from the International Centre for Diffraction Data (ICDD). The Raman spectra were acquired on a DXR Raman microscope (Thermo Scientific) with a 32-two-second scan, laser 532 nm laser (3 mW) under a 10 × objective of an Olympus microscope. The X-ray photoelectron spectroscopy (XPS) apparatus, comprising a SPECS PHOIBOS 100 hemispherical analyzer with a 5-channel detector and a SPECS XR50 achromatic X-ray source equipped with an Al and Mg double anode, was utilized to analyze the surface composition of the samples and the chemical states of the elements. Scanning electron microscopy (SEM) was conducted using an SEM/FIB Zeiss Crossbeam 350 (Germany). Energy-dispersive X-ray spectroscopy (EDX) was performed using an Ametek EDAX Octane Elite with an accelerating voltage of 7 kV to minimize the penetrating depth. Transmission electron microscopy (TEM) investigations were conducted utilizing the FEI Talos F200X microscope, operated at an accelerating voltage of 200 kV. EDX measurements were performed in scanning transmission electron microscope (STEM) mode employing a Super-X system with four SDDs. The specimen for TEM investigations was suspended in ethanol and deposited onto amorphous carbon, which was embedded on a Cu grid (Pacific Grid 300 mesh).

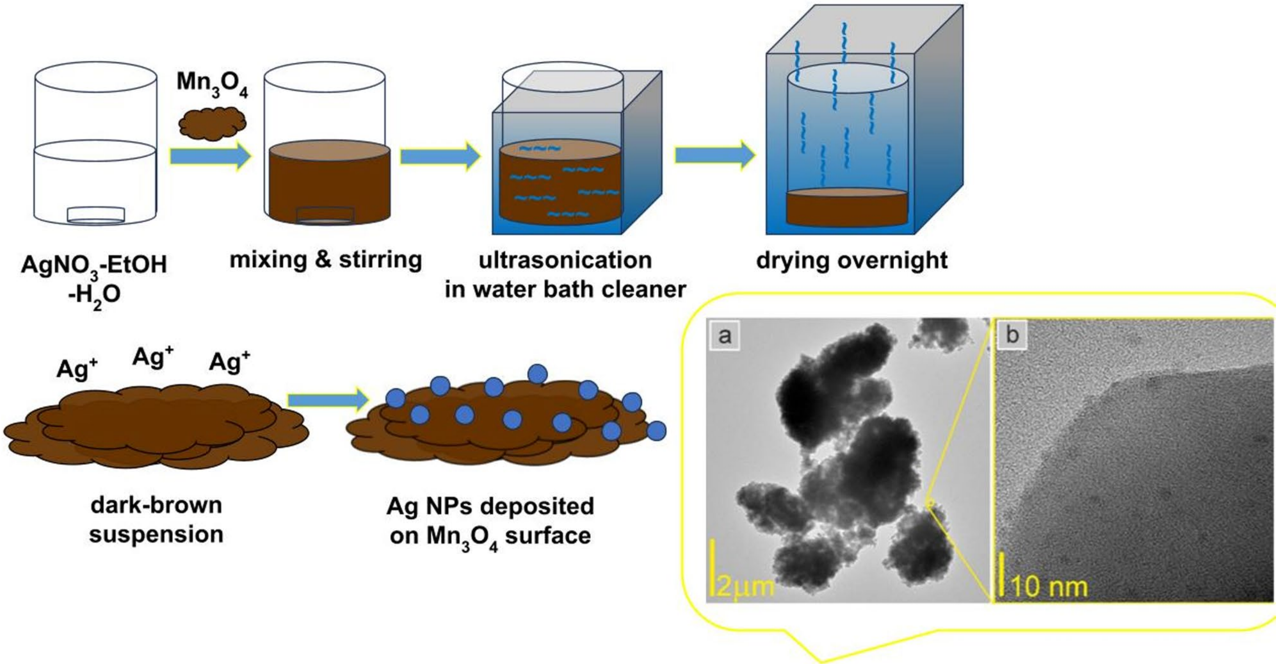

Fig. 1. The preparation process of Mn_3O_4@Ag composites with the proposed mechanism of reduction of $AgNO_3$ without the need for a reducing agent.

Preparation of electrodes and electrochemical measurements

The electrodes were prepared using M0, M1, M3, and M5 materials. To fabricate the working electrodes, the prepared active (M0, M1, M3, and M5) material (80 wt%), activated carbon (10 wt%), and poly (vinylidene) fluoride as binder (10 wt%) were thoroughly mixed. A homogeneous slurry of the above materials was made by using acetone as a common solvent. The prepared slurry was brush-coated over activated carbon cloth (AVCarb, USA) with a geometric area of ~ 1 cm^2, and allowed the electrodes to evaporate at room temperature (RT) for ~ 7 h for the removal of solvent (acetone in the present case). The loading mass on the electrodes was between 3.3 mg and 6.3 mg. Figure 2 shows the schematic illustration of the electrode fabrication process. The electrodes were tested in a two-electrode set-up using PVdF-HFP-PC-Mg(ClO_4)$_2$ as gel polymer electrolytes[18]. The cells were prepared by sandwiching a gel polymer electrolyte is placed between two symmetrical electrodes. To evaluate the electrochemical performance of the cell, cyclic voltammetry (CV) (at different scan rates and in the potential range from 0 to 1.4 V), ac impedance spectroscopy (frequency range from 200 kHz to 10 kHz), galvanostatic charge-discharge testing with repetitive cyclic testing (varying current density and in the potential range from 0 to 1.4 V). All the electrochemical measurements were carried out using a BioLogic VMP3 electrochemical workstation. Below is the configuration of the cells:

Cell A: M0 | PVdF-HFP-PC-Mg (ClO_4)$_2$ | M0.
Cell B: M1 | PVdF-HFP-PC-Mg (ClO_4)$_2$ | M1.
Cell C: M3 | PVdF-HFP-PC-Mg (ClO_4)$_2$ | M3.
Cell D: M5 | PVdF-HFP-PC-Mg (ClO_4)$_2$ | M5.

All the cells were rested for 4–5 h before electrochemical measurements, which ensured the enhanced electrochemical performance of the cells because of proper soaking of electrodes and electrolytes.

Results and discussion

Structural and morphological characterization of Mn_3O_4@Ag composites

As illustrated in Fig. 3a, the XRD patterns of the pristine (M0), and Ag-modified Mn_3O_4 (M1, M3, and (M5) powders exhibit a high degree of similarity to the tetragonal phase spinel-like Mn_3O_4 pattern (JCPDS card no. 24–0734)[19–22], thereby confirming that the modification of the surface using Ag nanoparticles does not result in phase segregation. As shown in Fig. 3a, the twelve characteristic XRD peaks of Mn_3O_4/Ag powders, observed at 2θ angles of 18.1°, 28.9°, 31.1°, 32.3°, 36.1°, 38.1°, 44.5°, 50.8°, 54.1°, 55.9°, 58.6°, and 59.9°, correspond to the (101), (112), (200), (103), (211), (004), (220), (105), (312), (303), (321), and (224) crystal planes of tetragonal Mn_3O_4, with lattice constants a = 5.76 Å, c = 9.47 Å, and space group I41/amd (Hausmannite, JCPDS card no. 24–0734)[19–22]. The peaks observed at 38° and 44° are attributed to the overlapping phases of Mn_3O_4 (004) and (220), as well as Ag (111) and (200). A simplified form of the Scherrer equation was employed to estimate the average crystallite size of Mn_3O_4 in pristine and in each Ag-modified material. The average crystallite size of Mn_3O_4 was found to be approximately 33 nm.

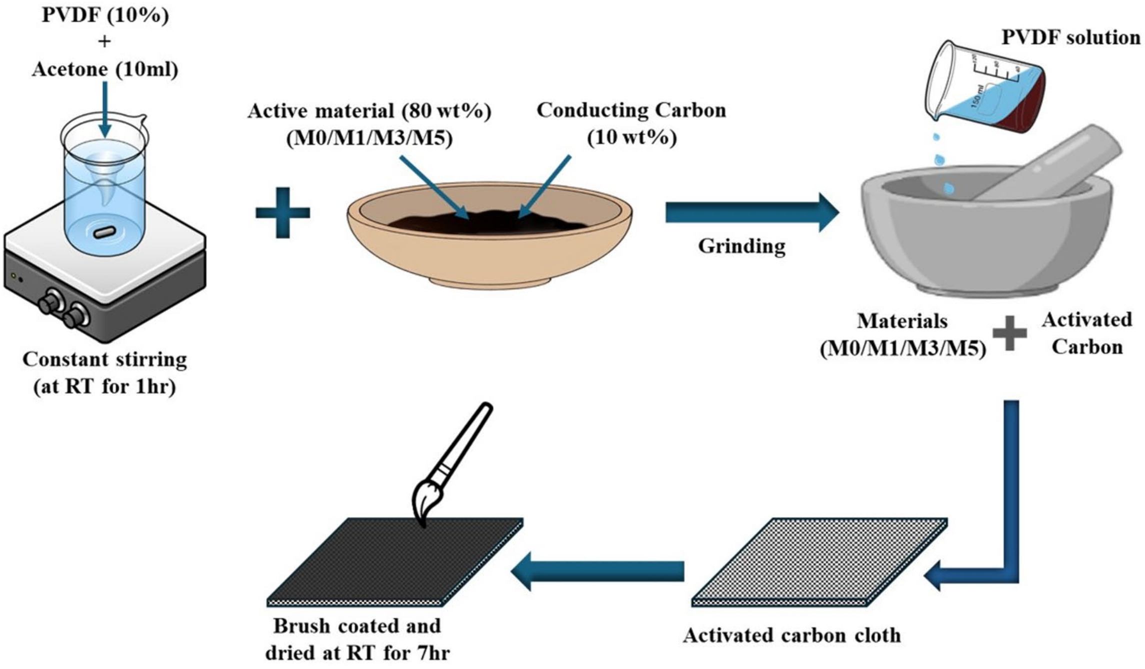

Fig. 2. Schematic illustration of the electrode fabrication process.

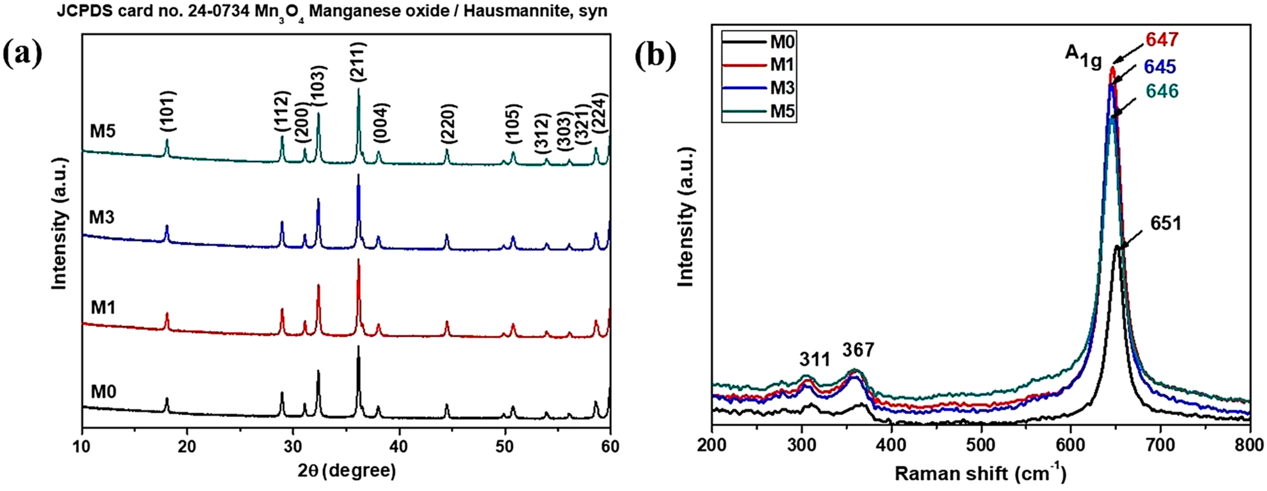

Fig. 3. The XRD pattern (**a**) and Raman spectra (**b**) of M0, M1, M3, and M5 samples.

It is important to note that interesting findings were obtained from Raman spectroscopy (Fig. 3b). The Raman spectra of each Mn_3O_4 sample were recorded in the range of 200 to 800 cm^{-1}. Furthermore, close observation of the Raman spectra of Mn_3O_4 samples surface-modified with Ag nanoparticles (M1, M3, and M5) reveals a strong alignment with the unmodified Mn_3O_4 sample (M0), as demonstrated in Fig. 3b. As shown in Fig. 3b, a sharp active band located at ~651 cm^{-1} was observed for all samples. This observation serves to confirm the crystalline nature of the samples analyzed, corresponding to the Mn–O stretching vibrations of divalent manganese ions (Mn^{2+}) in the coordination of the tetrahedral (MnO_6)[20,22–24]. The vibrational mode (A_{1g}) at 651 cm^{-1} is a representative characteristic of the tetragonal structure of Mn_3O_4, found in the mineral hausmannite. Furthermore, the two broad weak bands observed at ~311 and ~367 cm^{-1} are attributed to the out-of-plane bending modes of Mn–O (the E_g symmetry mode) and the asymmetric stretch of the bridge oxygen species Mn–O–Mn, respectively[20,22–24]. It is important to note that all the peaks in the resulting spectrum are indicative of the tetragonal structure of Mn_3O_4. The results of the present study are in close alignment with those reported in the literature[20,22–24]. The surface modification of Mn_3O_4 powders by Ag in the 1–5%wt. the range does not result in any qualitative changes to the spectrum, thereby indicating that the tetragonal I41/amd symmetry remains unaltered. However, as the amount of silver used in the modification process increased, an increase in the intensity of the A_{1g} peaks and a shift of ~ 5 cm^{-1} was observed in the M1, M3, and M5 samples, compared to the pristine Mn_3O_4 material. It is recognized that Ag particles can trigger a surface-enhanced Raman scattering effect[25].

The X-ray photoelectron spectroscopy (XPS) analysis revealed the presence of Mn and O in the M0 and M3 samples, with Ag, and C detected exclusively in the M3 sample (refer to survey XPS spectra Fig. 4a). The high-resolution spectra for Mn 2p, O 1s, and Ag 3d from the M3 sample are presented in Fig. 4b-d. Specifically, Fig. 4b illustrates the XPS spectrum of Mn 2p, where two peaks at 641.1 eV and 652.8 eV correspond to the Mn $2p_{3/2}$ and Mn $2p_{1/2}$ levels, respectively. The band gap energy difference between these two peaks, 11.7 eV, further supports the presence of Mn_3O_4[26–29]. Furthermore, analysis of the asymmetric O 1s peak (Fig. 4c) revealed two primary components: one at 530.0 eV, attributed to Mn–O bonding within the spinel Mn_3O_4 structure (with Mn^{2+} in MnO and Mn^{3+} in Mn_2O_3), and another at 532.0 eV, indicative of chemisorbed oxygen on the surface of the spinel crystallites[26–29]. Moreover, the XPS results demonstrate that the deposition of Ag is an effective process, with the metallic silver phase being identified on the Mn_3O_4 surface (see Fig. 4d). The binding energies of 368.1 eV and 374.1 eV correspond to the Ag $3d_{5/2}$ and Ag $3d_{3/2}$ peaks of metallic silver[17], respectively.

The morphology of all samples (M0, M1, M3, and M5) was examined using scanning electron microscopy (SEM) (refer to Fig. 5). For selected sample M3, which exhibited the most favourable electrochemical performance, transmission electron microscopy (TEM) techniques were employed (refer to Fig. 6). SEM analysis of the pristine Mn_3O_4 (M0) sample revealed particles with irregular shapes and rough surfaces. These particles were densely aggregated with minimal visible porosity, and their sizes ranged from approximately 1 to 3 µm. The addition of Ag (samples: M1, M3. M5) led to a noticeable alteration of the Mn_3O_4 surface, characterized by increased granularity and irregularity as the Ag content increased. While the pristine Mn_3O_4 particles maintained their size range of 1 to 3 µm, the presence of Ag nanoparticles, less than 500 nm in size, became increasingly evident in samples with higher Ag content (M3 and M5). The higher-resolution SEM images for M1, M3, and M5 samples (see Fig. S1 in the Supplementary Material) reveal a clear visualization of the surface morphology and serve to confirm the presence of metallic Ag nanoparticles on the Mn_3O_4 surface, existing as small spherical structures. As the Ag content increases from 1 to 5%, there is an observable shift in the distribution of the nanoparticles, which become more densely distributed and slightly larger (a tendency towards agglomeration is also evident). Notably, sample M5 exhibits the most uniform and abundant coverage.

In order to verify the presence of Ag nanoparticles in each surface-modified sample, an EDS analysis was performed, and the results are provided in the Supplementary Material (refer to Fig. S2–S5). The analysis indicated that Ag was present in its metallic form (Fig. S2–S5). To gain a deeper understanding of the sample

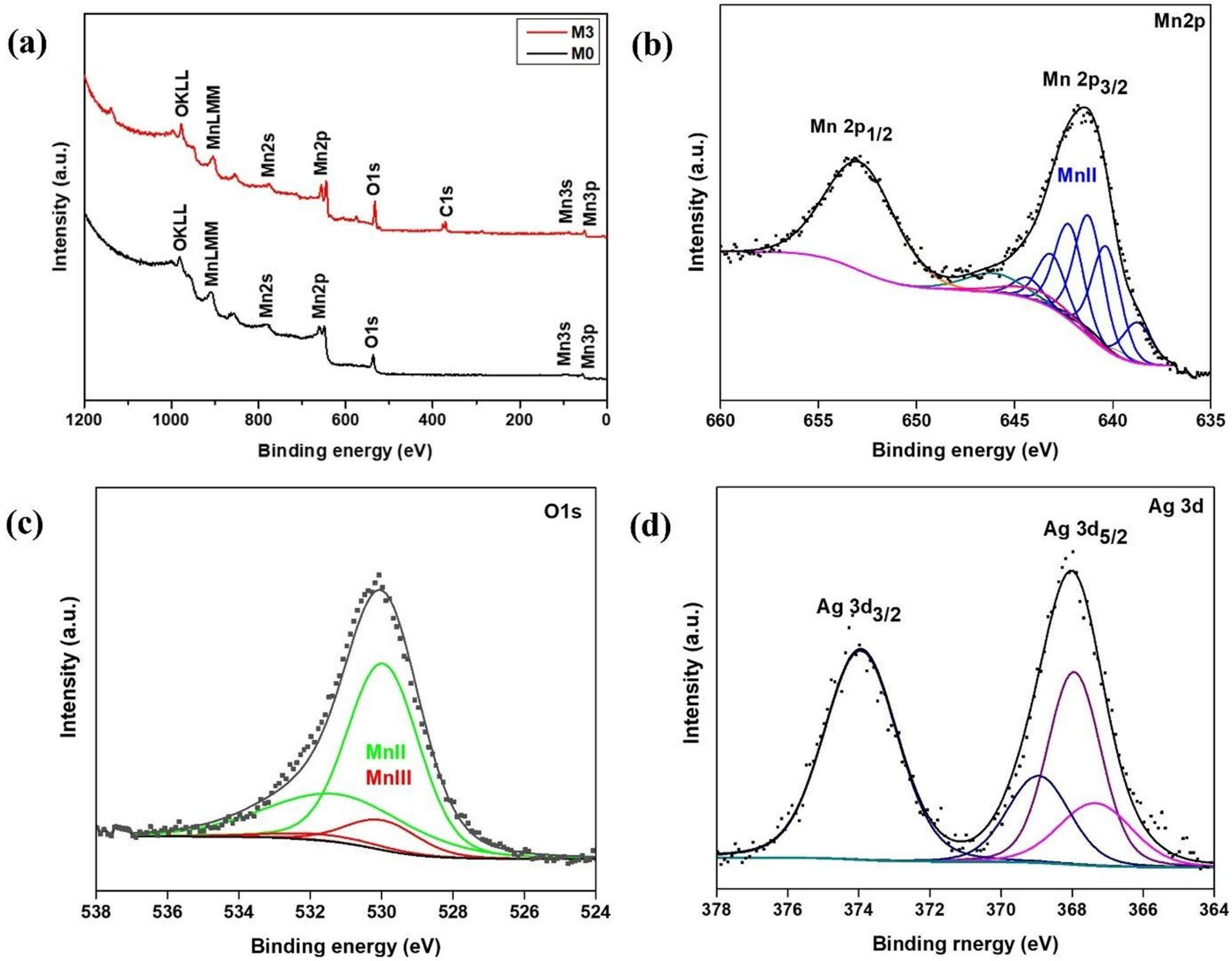

Fig. 4. XPS survey spectra of M0 and M1 samples (**a**), high-resolution spectra of Mn 2p (**b**), O 1s (**c**), and Ag 3d (**d**) of M3 sample.

morphology, the presence of Ag, and to obtain information about the average size of Ag, TEM measurements were conducted for sample M3 with a three-weight content of Ag (see Fig. 6).

As demonstrated in Fig. 6, the TEM analysis of sample M3, which consists of Mn_3O_4 powder, confirmed the presence of Ag on the surface. Figure 6b clearly shows the presence of crystalline silver nanoparticles. To determine the distribution of silver particles on the analyzed sample, elemental mapping (HAADF-EDX) of Mn, O, and Ag was conducted (see Figs. 6c-h). The mapping results are presented in a series of images in Figs. 6(e, f, and h), indicating a uniform and well-distributed Ag NPs on the Mn_3O_4 surface. Additionally, the Mn_3O_4 surface exhibited excellent coverage by Ag nanoparticles as highlighted in Figs. 6(e, f and h). The generation of a histogram of the silver nanoparticle sizes was facilitated by the TEM images, as demonstrated in Fig. 6i. The application of a LogNormal distribution to the data yielded an average silver nanoparticle diameter of Xc = 2.2 nm.

Furthermore, the nitrogen adsorption-desorption isotherms have been recorded for all samples and are provided and discussed in the Supplementary Material (Fig. S6 and Table S1).

Electrochemical evaluation of Mn_3O_4@Ag composites

The pristine Mn_3O_4 and Ag-surface modified Mn_3O_4 electrodes (M0, M1, M3, and M5) were tested and evaluated as electrode materials for supercapacitors in a two-electrode system using magnesium ion-based gel polymer electrolyte. The cells mentioned above (Cell A-Cell D) were first tested using cyclic voltammetry (CV) at different scan rates in the potential range from 0 to 1.4 V. The CV curves of all cells at a scan rate of 5 mV s^{-1} and in the potential range from 0 to 1.4 V are shown in Fig. 7a. As can be seen from the curves, cell A exhibits a symmetrical curve without any significant redox peaks, but in the case of cell B-cell D, redox peaks have been observed, it is due to the introduction of silver nanoparticles in the manganese oxide network. In order to understand the scenario, the electrochemical reaction between Mn_3O_4 and silver nanoparticles involves the transfer of electrons between the two, wherein Mn_3O_4 acts as an oxidizing agent and silver will act as a reducing agent and hence silver in the Mn_3O_4 network is interesting for electrochemical applications particularly to increase the stability of the cells. All the curves are reversible and hence show excellent reversibility of the redox

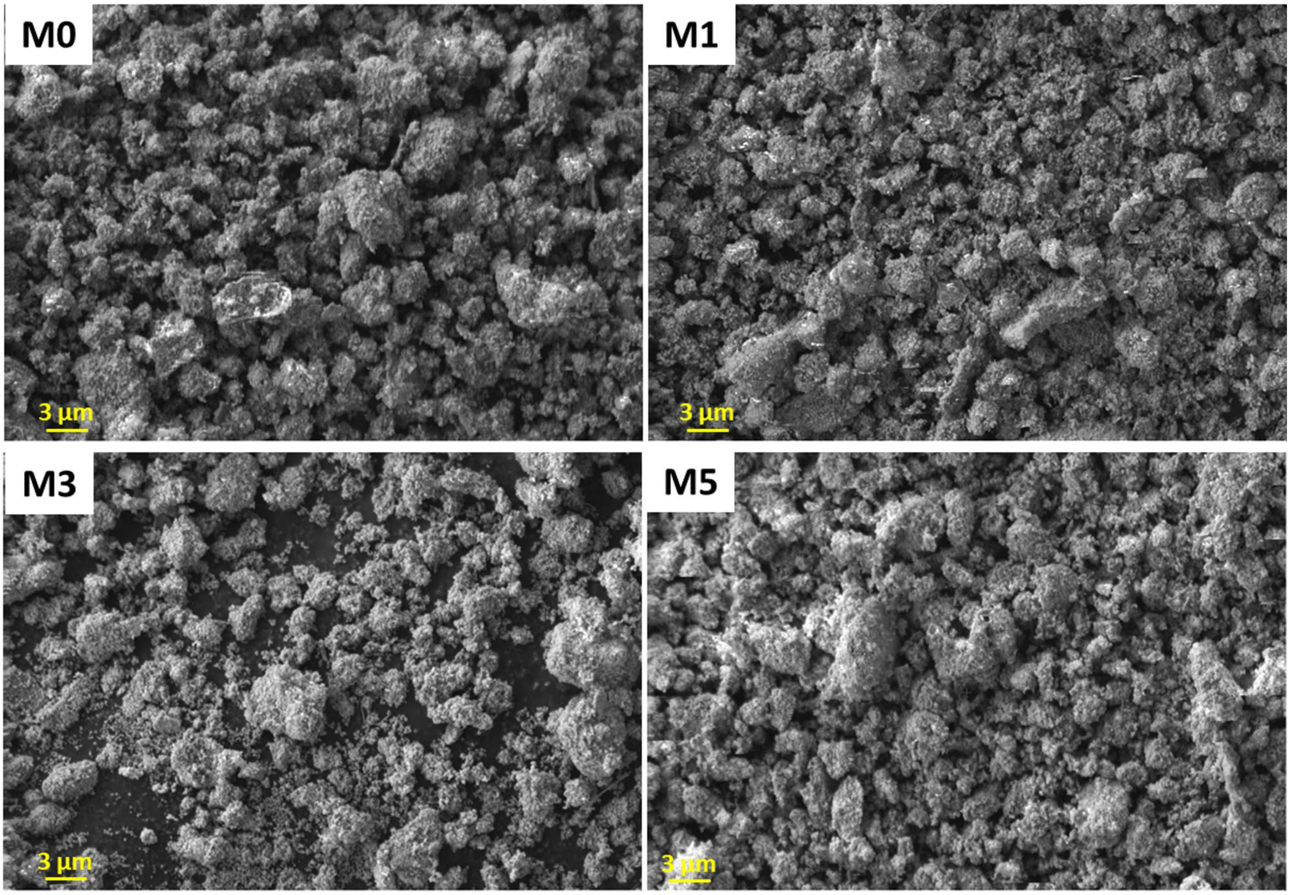

Fig. 5. SEM images of M0, M1, M3, and M5 samples. Magnification: 2.5 KX. (scale bar 3 µm).

processes. Also from the figures, it can be clearly seen that cell C exhibits the highest sweep area which clearly means that the cell has higher capacitance and lower resistance as compared to other cells. The capacitance values of cell A have been calculated using equation S1, whereas for cell B-cell D, the capacitance values were calculated using the Trasatti method (equation S2), the equations are provided in the Supplementary Material. The specific capacitance of a single electrode has been found to be of the order of ~ 8.31 F g^{-1}. Figure 7b shows the CV curves of cell C at different scan rates, viz. 5, 10, 20, 30, 50, 100 mV s^{-1} in the potential range from 0 to 1.0 V, the rate capability of the cell is very good, and the deviation of CV curves from the ideal capacitive curves are mainly due to the contribution caused by redox reaction. Additionally, with the increase in the scan rates, the CV curves are smooth and free from redox peaks, it is mainly due to the fast switching in and out of ions, hence receiving less time for the redox reactions. Figure 7c shows the variation of specific capacitance with respect to scan rates, as can be seen from the figure, the cell follows the standard behavior and with the increase in scan rates, capacitance values gradually decreases which is clearly due to the insufficient time for the electrolyte ions (Mg^{2+} and ClO_4^-) to switch in and out of ions and hence there are incomplete electrochemical reactions leading to the reduced capacitance of the cells.

The relationship between peak current (I) and scan rate (V) provides insight into the dominant electrochemical mechanisms within the electrode[30]. By plotting log(I) versus log(V) (Figure S7) for low scan rates (5–100 mV s^{-1}), the slope of the plot can be used to predict the charge storage mechanism. A slope value of 0.5 indicates that the process is diffusion-controlled, whereas a slope of 1 signifies capacitive contributions[31]. When the slope lies between 0.5 and 1, it suggests a mixed mechanism involving both capacitive and diffusion-controlled processes[32]. In the case of cell C, the slope value was determined to be 0.57, indicating that the total charge storage is derived from a combination of capacitive and diffusion-controlled mechanisms. The individual contributions of these mechanisms can be calculated using specific equations S6, S7, and S8 given in the supporting information and the Fig. 7d illustrates the variation in capacitive (Q_s) and diffusion-controlled (Q_d) charge contributions at different scan rates. At a low scan rate of 5 mV/s, the extended time available for ion movement allows ions to diffuse deeply into the bulk of the electrode material, resulting in a higher diffusion-controlled contribution (Q_d=68.54%) compared to the capacitive contribution (Q_s=31.46%). As the scan rate increases, the time for ion diffusion becomes limited, leading to surface-dependent capacitive processes where charge is stored electrostatically or through rapid redox reactions at the surface. The capacitive contribution significantly increases to 74.17%, while the diffusion-controlled contribution decreases to 25.83%.

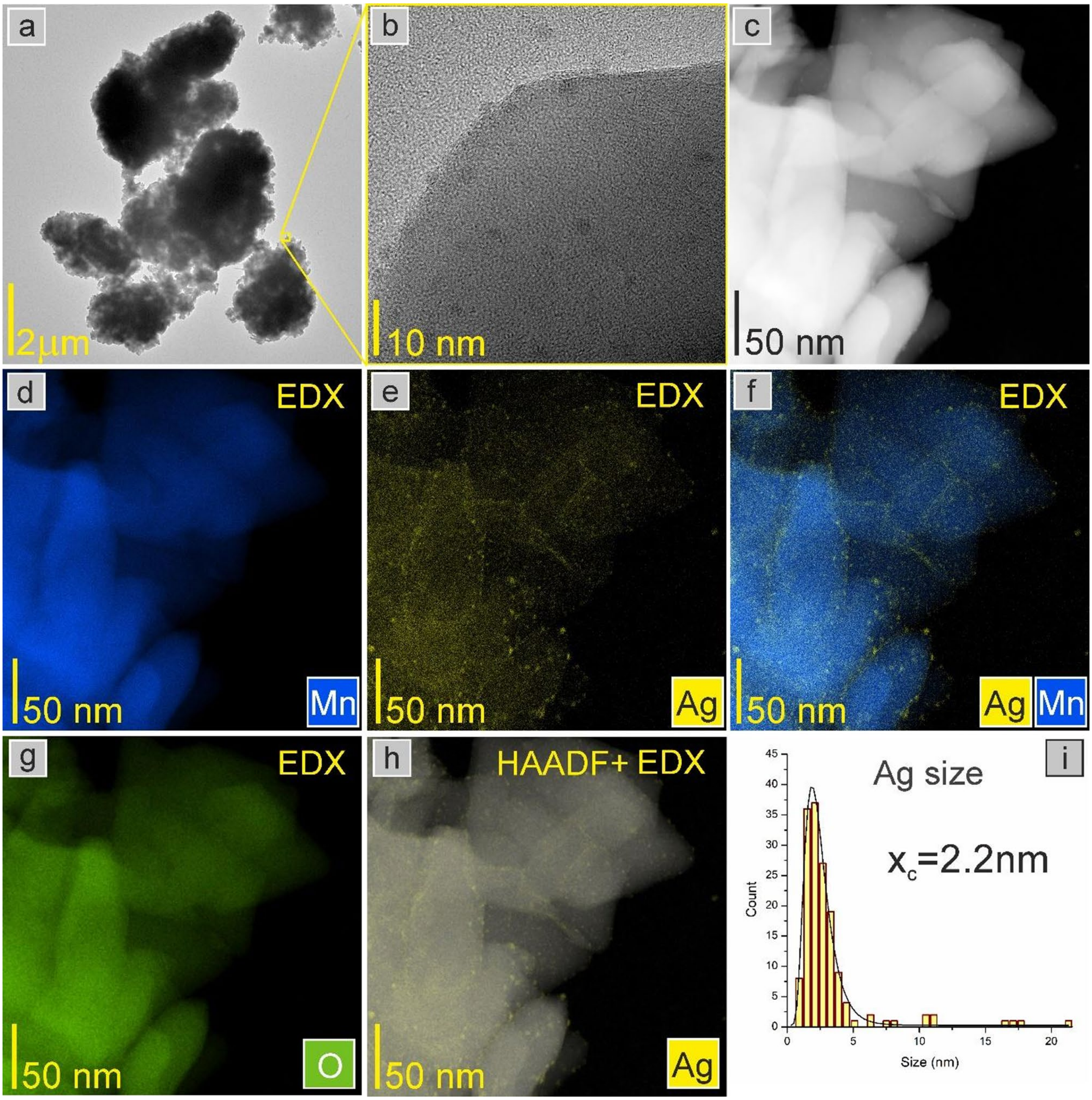

Fig. 6. (**a**) TEM image of the sample M3, (**b**) with a zoomed-in view showing a deposition of the Ag NPs, (**c**) HAADF image, (**d**-**g**) EDX mapping of Mn, Ag, O, (**h**) HAADF with EDX image of Ag NPs, and (**i**) histogram of the silver nanoparticle size.

Figure 8a shows the representative impedance spectroscopy curves of cell A-cell D, which also reveal the impact of adding silver in the Mn_3O_4 network. Following the CV results, three weight percentages of silver nanoparticles in the electrode network show the best electrochemical performance. It was also found out that charge transfer resistance is the least for cell C as compared to other cells, and hence the capacitance value is the highest (8.32 F g^{-1}). The capacitance values are calculated by using equation S3 (provided in supplementary information). It signifies that 3 wt% of silver is optimized, and it also slows the resistance between the electrode and electrolytes. To further confirm the electrochemical results, galvanostatic charge-discharge (GCD) studies have been carried out for all cells at a current density of 0.058 A g^{-1}, and in the potential window of 0 to 1.4 V. The results have been shown in Fig. 8b. As can be seen, GCD curves show the redox nature of prepared electrodes, and the results are in-line with other electrochemical results mentioned above. The specific capacitance of cells was found to be of the order of 9.38 F g^{-1}, with an energy density of 1.9 Wh kg^{-1} and power density of 30.8 W kg$^{-1,}$ respectively. Figure 8c shows the GCD curves of cell C at different current densities and in the potential window of 0 to 1.0 V. Table S2 shows the literature comparison of Mn_3O_4 material and its composites for supercapacitor

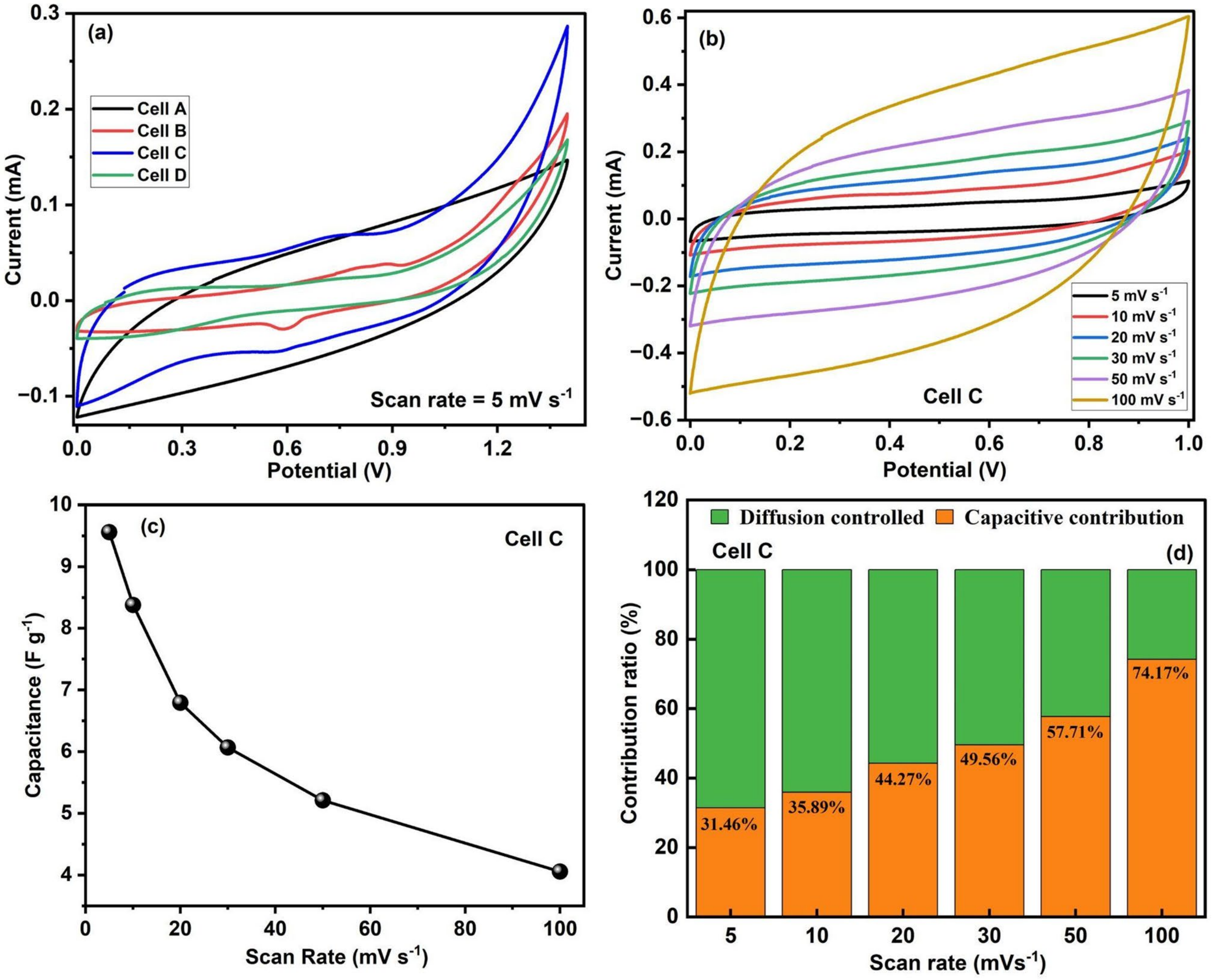

Fig. 7. (**a**) Cyclic voltammetry curves of cell A-cell D at a scan rate of 5 mV s^{-1}, (**b**) cyclic voltammetry curve of cell C at different scan rates, (**c**) variation of specific capacitance of cell C with respect to different scan rates and (**d**) Capacitive and diffusion-controlled charge contributions of cell C at scan rates of 5 and 100 mV/s.

application. It is important to highlight that this study introduces a simple, cost-effective, and environmentally friendly method for depositing Ag nanoparticles onto the Mn_3O_4 surface without the use of any reducing agents. Notably, this work presents, for the first time, the investigation of the Mn_3O_4@Ag composite in the fabrication of a symmetrical supercapacitor cell incorporating a gel polymer electrolyte. As can be seen from the graphs that at lower current density, the cells show higher capacitance, it is potentially due to the facile diffusion of protons through the manganese network, at lower current densities it is easier for the protons to infiltrate into the inner cores of the network unlike at higher current densities where the ions only interact with outer surface of the electrode, thereby decreasing the capacitance of the cells. Figure 8d shows the long-term cyclic stability performance of cell C to check the chemical stability of the prepared materials. It is worth noting that in the case of supercapacitors, the electrodes are in direct contact with electrolyte materials, and the stability of electrodes in such cases is critically important, and it can be tested by performing long-term cyclic testing. Cell C was cycled continuously for ~ 15,000 galvanostatic cycles in the potential window from 0 to 1.0 V and at a current density of 0.058 A g^{-1}. The cell was stable throughout cyclic testing; in fact, the capacitance was increased by almost double after cycling testing, clearly confirming the chemical stability of the M3 material. Additionally, the coulombic efficiency was also nearly 100% throughout the cycles. The SEM characterization with EDX (Fig. S8, Fig. S9) reveals the morphological stability of the materials. Also, from micro-images, the presence of electrolyte ions is confirmed, which may be attached to the electrode materials during charging and discharging measurements.

Conclusion

This work presents a pioneering application of a gel polymer electrolyte (GPE) for supercapacitor technology, utilizing a novel combination of PVdF-HFP as the host polymer, propylene carbonate (PC) as the plasticizer, and magnesium perchlorate ($Mg(ClO_4)_2$) as the salt, in conjunction with Ag nanoparticle (NP)-modified Mn_3O_4 electrodes. The study demonstrates the successful use of this GPE and electrode configuration in a two-electrode

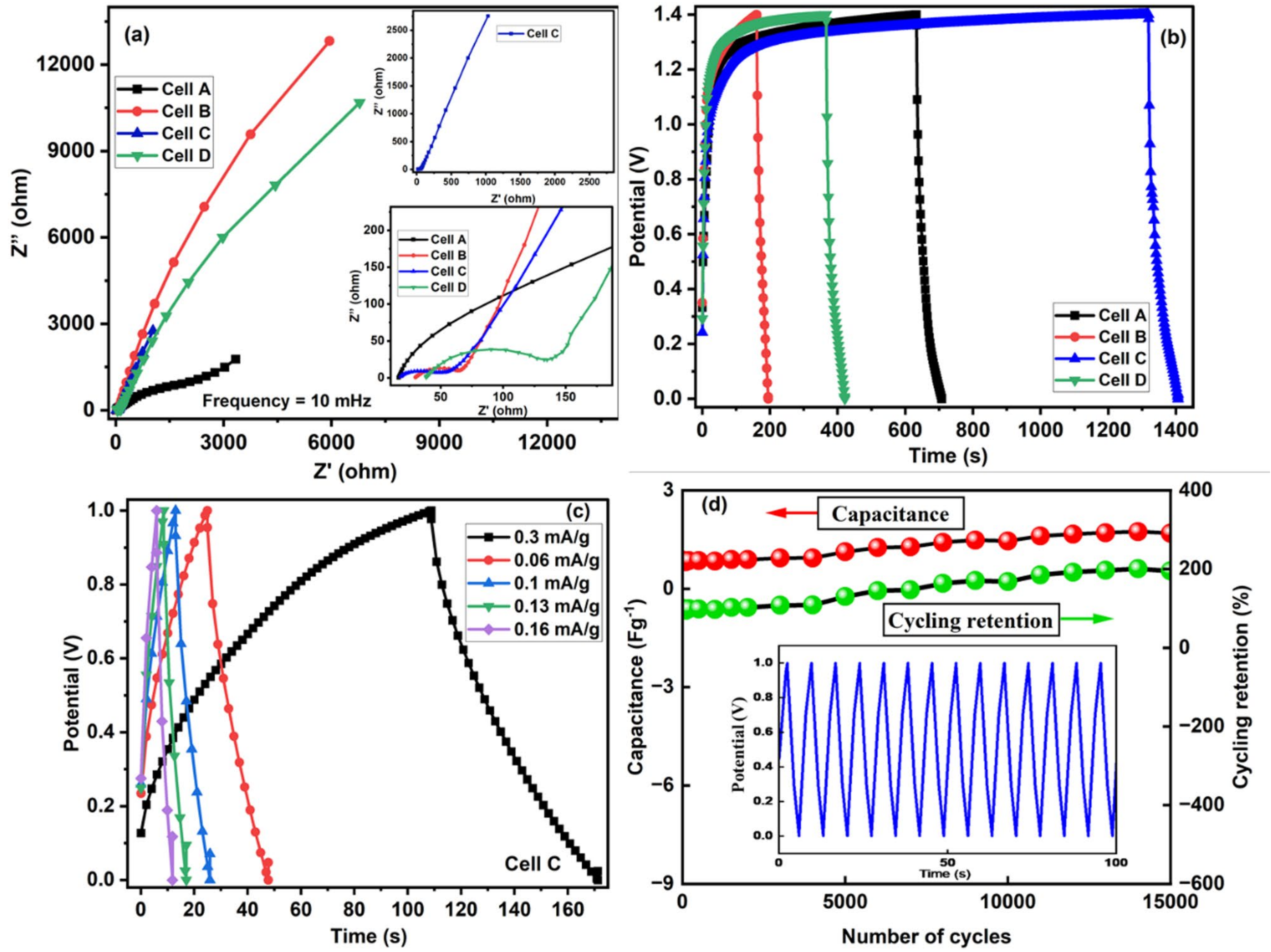

Fig. 8. (**a**) Electrochemical impedance spectroscopy curves of cell A-cell D at a frequency of 10 mHz, (**b**) galvanostatic charge discharge curves of cell A-cell D, (**c**) galvanostatic charge discharge curves of cell C at different current densities and (**d**) cyclic testing and cyclic retention of cell C at a current density of 0.058 A g^{-1} (inset shows the few cycles).

supercapacitor system, achieving a specific capacitance of 9.38 F g^{-1} and excellent energy and power densities of 1.9 Wh kg^{-1} and 30.8 W kg^{-1}, respectively. Notably, the supercapacitor cells exhibited outstanding stability, retaining high performance over approximately 10,000 charge-discharge cycles at a current density of 0.058 A g^{-1}. The incorporation of silver nanoparticles within the Mn_3O_4 electrodes significantly enhanced the capacitive performance, underscoring their potential for energy storage applications. The study also introduces a novel, low-temperature ultrasonication method for attaching Ag NPs to Mn_3O_4. This method is simple, cost-effective, and scalable, and eliminates the need for a reducing agent, offering a promising and sustainable method for future supercapacitor manufacturing. The research contributes significantly to energy storage technologies, providing valuable insights for the development of high-performance, scalable supercapacitor systems.

Data availability

The data will be available on the request from the corresponding author (Dr. Monika Michalska, monika.kinga.michalska@gmail.com).

Received: 6 February 2025; Accepted: 27 May 2025

References

1. Zhang, J., Gu, M. & Chen, X. Supercapacitors for renewable energy applications: A review. *Micro Nano Eng.* **21**, 100229 (2023).
2. González, A., Goikolea, E., Barrena, J. A. & Mysyk, R. Review on supercapacitors: technologies and materials. *Renew. Sustain. Energy Rev.* **58**, 1189–1206 (2016).
3. Reenu, Sonia, L., Phor, A., Kumar, S. & Chahal Electrode materials for supercapacitors: A comprehensive review of advancements and performance. *J. Energy Storage.* **84**, 110698 (2024).
4. Zhang, Y. et al. Progress of electrochemical capacitor electrode materials: A review. *Int. J. Hydrog Energ.* **34**, 4889–4899 (2009).

5. Jain, A. et al. Utilization of compressible hydrogels as electrolyte materials for supercapacitor applications. *RSC Adv.* **13**, 11503–11512 (2023).
6. Jain, A. et al. Vanadium oxide nanorods as an electrode material for solid state supercapacitor. *Sci. Rep.* **12**, 1–12 (2022).
7. Jiang, J. & Kucernak, A. Electrochemical supercapacitor material based on manganese oxide: Preparation and characterization. *Electrochim. Acta*. **47**, 2381–2386 (2002).
8. Beknalkar, S. A. et al. Mn_3O_4 based materials for electrochemical supercapacitors: basic principles, charge storage mechanism, progress, and perspectives. *J. Mater. Sci. Technol.* **130**, 227–248 (2022).
9. Li, D. et al. One-pot hydrothermal synthesis of Mn_3O_4 nanorods grown on Ni foam for high performance supercapacitor applications. *Nanoscale Res. Lett.* **8**, 535 (2013).
10. Raj, B. G. S., Asiri, A. M., Wu, J. J. & Anandan, S. Synthesis of Mn_3O_4 nanoparticles via chemical precipitation approach for supercapacitor application. *J. Alloys Compd.* **636**, 234–240 (2015).
11. Luo, Y., Yang, T., Li, Z., Xiao, B. & Zhang, M. High performance of Mn_3O_4 cubes for supercapacitor applications. *Mater. Lett.* **178**, 171–174 (2016).
12. Fang, Q. et al. Ultrafine Mn_3O_4 nanowires synthesized by colloidal method as electrode materials for supercapacitors with a wide voltage range. *J. Energy Storage*. **44**, 103260 (2021).
13. Cuéllar-Herrera, L. et al. Romero-Serrano, chemical synthesis and electrochemical performance of hausmannite Mn_3O_4/rGO composites for supercapacitor applications. *Int. J. Electrochem. Sci.* **19**, 100737 (2024).
14. Zhang, W. et al. High performance Flower-Like Mn_3O_4/rGO composite for supercapacitor applications. *J. Electroanal. Chem.* **910**, 116170 (2022).
15. Chinnaiah, K., Kannan, K., Chen, Y. S. & Gurushankar, K. Exploring Ag/Mn_3O_4 composite nanorods as an attractive battery-type electrode material for supercapacitors. *J. Phys. Chem. Solids*. **196**, 112310 (2025).
16. Jain, A., Michalska, M., Zaszczyńska, A. & Denis, P. Surface modification of activated carbon with silver nanoparticles for electrochemical double layer capacitors. *J. Energy Storage*. **54**, 105367 (2022).
17. Jain, A. & Michalska, M. Enhanced electrochemical properties of multiwalled carbon nanotubes modified with silver nanoparticles for energy storage application. *Mater. Chem. Phys.* **317**, 129200 (2024).
18. Tripathi, S. K., Jain, A., Gupta, A. & Mishra, M. Electrical and electrochemical studies on magnesium ion-based polymer gel electrolytes. *J. Solid State Electrochem.* **16**, 1799–1806 (2012).
19. Garcês Gonçalves, P. R. Jr, De Abreu, H. A. & Anderson Duarte, H. Stability, structural, and electronic properties of hausmannite (Mn_3O_4) surfaces and their interaction with water. *J. Phys. Chem. C*. **122**, 20841–20849 (2018).
20. Julien, C. M., Massot, M. & Poinsignon, C. Lattice vibrations of manganese oxides: part I. Periodic structures. *Spectrochim. Acta Part A Mol. Biomol. Spectrosc.* **60**, 689–700 (2004).
21. Jiang, Z. et al. Facile Preparation of Mn_3O_4 Hollow microspheres via reduction of pentachloropyridine and their performance in lithium-ion batteries. *RSC Adv.* **7**, 8264–8271 (2017).
22. Yusoff, N. F. M. et al. Electrochemical sodiation/desodiation into Mn_3O_4 nanoparticles. *ACS Omega*. **5**, 29158–29167 (2020).
23. Lan, D. et al. Synthesis, characterization and microwave transparent properties of Mn_3O_4 microspheres. *J. Mater. Sci.: Mater. Electron.* **30**, 8771–8776 (2019).
24. Wang, F. et al. Electrochemical properties of controlled size Mn_3O_4 nanoparticles for supercapacitor applications. *J. Nanosci. Nanotechnol.* **18**, 719–724 (2018).
25. Krajewski, M. et al. $Li_4Ti_5O_{12}$ modified with ag nanoparticles as an advanced anode material in lithium-ion batteries. *J. Power Sources*. **245**, 764–771 (2014).
26. Zahra, T. et al. Organic template-based ZnO embedded Mn_3O_4 nanoparticles: synthesis and evaluation of their electrochemical properties towards clean energy generation. *RSC Adv.* **10**, 9854–9867 (2020).
27. Ndouka, P. N. et al. Low-temperature catalytic methane deep oxidation over sol-gel derived mesoporous hausmannite (Mn_3O_4) spherical particles. **ChemPhysMater 3**, 329–340. (2024).
28. Shi, Y. et al. Catalysts for highly water-resistant catalytic decomposition of Ozone: hausmannite Mn_3O_4 on exposed (101) crystal surface. *J. Hazard. Mater.* **458**, 131947 (2023).
29. Pugazhvadivu, K. S. & Ashokkumar, M. Tuning the optical and magnetic properties of Mn_3O_4 quantum Dots by annealing process. *J. Mater. Sci.: Mater. Electron.* **35**, 830 (2024).
30. Vlad, A. et al. Hybrid supercapacitor-battery materials for fast electrochemical charge storage. *Sci. Rep.* **4**, 4315 (2014).
31. Gaire, M., Khatoon, N., Subedi, B. & Chrisey, D. Flexible iron oxide supercapacitor electrodes by photonic processing. *J. Mater. Res.* **36**, 4536–4546 (2020).
32. Kumar, C. et al. Opto-electrochemical variation with gel polymer electrolytes in transparent electrochemical capacitors for ionotronics. *Appl. Phys. Lett.* **124**, 111603 (2024).

Acknowledgements

Authors are thankful to Dr Kamil Bochenek (IPPT PAN) for SEM-EDX measurements. M. M. would like to thank Dr A. Malinowska (Łukasiewicz – IMiF) for the comparative discussion regarding XRD analysis. This work was financially supported by the Ministry of Education, Youth and Sports, Czech Republic (contract no. 8F21007), National Centre for Research and Development, Poland (V4-Japan/2/17/AtomDeC/2022) through the research project cooperation between the AtomDeC Consortium by funding received from the Visegrad group(V4)-Japan 2021 2nd Joint Call on "Advanced Materials". M.M. would like to acknowledge the financing support through the European Union under the REFRESH - Research Excellence For REgion Sustainability and High-tech Industries (project no. CZ.10.03.01/00/22_003/0000048) via the Operational Programme Just Transition. M. Michalska would like to thank for the assistance provided by the Research Infrastructure NanoEnviCz, supported by the Ministry of Education, Youth and Sports of the Czech Republic under Project No. LM2023066. This work was also supported by the VSB – Technical University of Ostrava (project No. SP2025/044).

Author contributions

M.M.: conceptualization, methodology, formal analysis, investigation, writing – original draft, writing – review & editing, resources, visualization, funding acquisition. M.S.: formal analysis, investigation, writing – original draft, visualization. J.S.: investigation. C.K.: investigation, writing – original draft. K.S.: formal analysis, investigation, writing – original draft. P.K.S.: formal analysis, writing – review and editing. A.J.: methodology, formal analysis, investigation, writing – original draft, writing – review & editing, resources, funding acquisition.

Declarations

Competing interests

The authors declare no competing interests.

Additional information

Supplementary Information The online version contains supplementary material available at https://doi.org/10.1038/s41598-025-04476-5.

Correspondence and requests for materials should be addressed to M.M. or A.J.

Reprints and permissions information is available at www.nature.com/reprints.

Publisher's note Springer Nature remains neutral with regard to jurisdictional claims in published maps and institutional affiliations.

Open Access This article is licensed under a Creative Commons Attribution-NonCommercial-NoDerivatives 4.0 International License, which permits any non-commercial use, sharing, distribution and reproduction in any medium or format, as long as you give appropriate credit to the original author(s) and the source, provide a link to the Creative Commons licence, and indicate if you modified the licensed material. You do not have permission under this licence to share adapted material derived from this article or parts of it. The images or other third party material in this article are included in the article's Creative Commons licence, unless indicated otherwise in a credit line to the material. If material is not included in the article's Creative Commons licence and your intended use is not permitted by statutory regulation or exceeds the permitted use, you will need to obtain permission directly from the copyright holder. To view a copy of this licence, visit http://creativecommons.org/licenses/by-nc-nd/4.0/.

© The Author(s) 2025